



Article

Efficient Charge Carrier Separation in L-Alanine Acids Derived N-TiO₂ Nanospheres: The Role of Oxygen Vacancies in Tetrahedral Ti⁴⁺ Sites

Yongjuan Chen, Xiu Luo, Yao Luo, Peiwen Xu, Jiao He, Liang Jiang, Junjie Li, Zhiying Yan and Jiaqiang Wang *

School of Chemical Sciences & Technology, National Center for International Research on Photoelectric and Energy Materials, Yunnan Provincial Collaborative Innovation Center of Green Chemistry for Lignite Energy, Yunnan Province Engineering Research Center of Photocatalytic Treatment of Industrial Wastewater, The Universities' Center for Photocatalytic Treatment of Pollutants in Yunnan Province, Yunnan University, Kunming 650091, China; chen Yongjuan@ynu.edu.cn (Y.C.); xiuluo@ynu.edu.cn (X.L.); LYjdt123@163.com (Y.L.); juneya@126.com (P.X.); hejiao@ynu.edu.cn (J.H.); liangjiang_ynu@163.com (L.J.); junjieli@ynu.edu.cn (J.L.); zhyyan@ynu.edu.cn (Z.Y.)

* Correspondence: jqwang@ynu.edu.cn; Tel.: +86-871-65031567

Received: 25 March 2019; Accepted: 29 April 2019; Published: 5 May 2019



Abstract: N-doped TiO₂ with oxygen vacancies exhibits many advantages for photocatalysis, such as enhanced visible light absorbency, inhibition of the photogenerated charge carrier recombination, etc. However, preparation of N-doped TiO₂ with oxygen vacancies under mild conditions is still a challenge. Herein, N-doped TiO₂ nanospheres with tetrahedral Ti⁴⁺ sites were synthesized by using dodecylamine as template and assisted by L-alanine acids. The obtained samples were characterized by X-ray powder diffraction (XRD), scanning electron microscopy (SEM), transmission electron microscopy (TEM), and UV–Vis diffuse reflectance spectra (UV–Vis DRS). It was found that the dodecylamine as a neutral surfactant controlled the structure of TiO₂ spherical, while L-alanine acids provided a nitrogen source. The existence of tetrahedral Ti⁴⁺ sites in N-doped TiO₂ was also confirmed. The N-doped TiO₂ sample with tetrahedral Ti⁴⁺ sites exhibited significantly improved photocatalytic performance for degradation of methylene blue solution under UV light or visible light irradiation. A combined time-resolved infrared (IR) spectroscopy study reveals that the enhanced photocatalytic performance could be attributed to a large amount of photogenerated charge carriers and efficient charge separation. It is demonstrated that the shallow donor state produced by oxygen vacancies of tetrahedral Ti⁴⁺ sites can effectively promote separation of charge carriers besides capturing electrons.

Keywords: N-doped TiO₂; tetrahedral Ti⁴⁺ sites; photocatalytic; L-alanine acids; time-resolved IR spectroscopy

1. Introduction

TiO₂-based photocatalysts have been most widely investigated in the past decades. However, practical applications of TiO₂ are still very limited because its fast recombination of photogenerated electron-hole pairs and wide band gap (3.2 eV) lead to a low quantum efficiency of photocatalytic reaction. Various strategies have been developed for improving the photocatalytic activities of TiO₂ based photocatalysts, such as combined with a semiconductor, metal ion/nonmetal doping, deposition with noble metal on surface, dyes sensitization, and defect creation [1]. Doping of TiO₂ with nitrogen was considered as a promising approach to improve photocatalytic activity for TiO₂ under visible light [2]. A number of strategies can be used to prepare N-doped TiO₂, for example, sputtering [3], ion implantation [4], chemical treatments of TiO₂ [5], sol–gel process [6], thermal oxidation from TiN [7],

etc. The sol–gel method is usually preferred because doping amount of N and the size of the sample can be easily controlled [8]. In this doping process, some specific acid or alkali additives can act as a cotemplate along with surfactants/polymer assemblies and this may play a significant role in precisely tailoring both TiO₂ structure and morphology [9]. Kanie et al. [10] found that ammonia and primary amines are more likely to make TiO₂ generate elliptical particles in gel–sol process. Durupthy et al. [11] also demonstrated the presence of the amino acids has an effect on the kinetics and thermodynamics during the crystalline TiO₂ formation. These accomplishments have inspired us to use amino acids in preparing N-doped TiO₂ with unique structure, and amino acids can also serve as good sources of nitrogen.

In process of N-doping, oxygen vacancies often occur in the lattice of titanium dioxide [12,13]. The stability of surface oxygen vacancies may lead to improvement of photocatalytic activity. Krol et al. [14] revealed that coordination geometry, from an octahedral to a tetrahedral of Ti⁴⁺ in TiO₂, can be adjusted by generating a large number of stable oxygen vacancies. Gray et al. [15] also confirmed that the tetrahedral Ti⁴⁺ sites contribute to the increased photoactivity. Therefore, the construction of tetrahedral Ti⁴⁺ sites is also an effective strategy to produce stable oxygen vacancies. But treatment at high-temperature by used reducing gases (e.g., NH₃ [16] and H₂ [17]) is required. Thus, it is still a challenge to develop synthetic strategy of tetrahedral Ti⁴⁺ sites under mild conditions and exploiting their unique properties for photocatalytic applications.

Herein, we describe a new and facile chemical process to synthesize N-doped TiO₂ nanospheres with tetrahedral Ti⁴⁺ sites using dodecylamine as template and assisted by L-alanine acids. The photocatalytic performance of the obtained samples was measured by photodegradation of methylene blue (MB) under UV and visible light irradiation. The sample with tetrahedral Ti⁴⁺ sites in N-doped TiO₂ exhibited significantly photocatalytic performance, whether under UV light or visible light.

2. Materials and Methods

2.1. Synthesis of Samples

All reagents were analytical grade and used without further purification. In a typical synthesis [18], 1.83 g dodecylamine (DDA, Sinopharm Chemical Reagent Co., Ltd., Shanghai, China) was dissolved in 30 mL absolute ethyl alcohol, and 3.21 g titanium tetraisopropoxide (TTIP, ≥97%, Sigma-Aldrich, St. Louis, MO, USA) was then added slowly in this solution. Subsequently, 60 mL L-alanine acids (Ala, Sinopharm Chemical Reagent Co., Ltd., Shanghai, China) solution (0.187 mol·L⁻¹) was added dropwise stirring at 333 K for 24 h. The final mixture was transferred into a Teflon bottle (250 mL) and heated at 363 K for 96 h under autogenous pressure. After the autoclave was cooled to room temperature, the slurry was filtered and washed with deionized water for several times. Finally the product was calcined at 673 K for 4 h in muffle furnace. The obtained example was denoted as MTiO₂/Ala-DDA (M represents mesoporous). A similar procedure was applied in the preparation of MTiO₂ and MTiO₂/Ala in the absence of L-alanine acids (Ala) and dodecylamine (DDA), respectively.

2.2. Characterizations

X-ray powder diffraction (XRD) experiments were carried out using a Rigaku TTRIII X-ray diffractometer (Rigaku D/max-3B, Tokyo, Japan) with Cu K_α radiation. The Brunauer–Emmett–Teller (BET) surface area was measured on a Micromeritics Tristar II Surface Area and Porosity Analyzer (Micromeritics, Norcross, GA, USA). A pore size distribution was obtained by Barrett–Joyner–Halenda (BJH) method using nitrogen desorption data measured at 77 K. Scanning electron microscopy (SEM) images were taken by FEIQuanta200FEG microscope (FEI, Eindhoven, The Netherlands) at an accelerating voltage of 15 kV. The transmission electron microscopy (TEM) and high-resolution transmission electron microscopy (HRTEM) images were obtained by JEM Fas-TEM-3010 electron microscope instrument (JEOL, Tokyo, Japan) at the accelerating voltage of 200 kV. UV–Vis diffuse

reflectance spectra (UV–Vis DRS) were measured by UV-2401PC photometer (Shimadzu, Kyoto, Japan) using BaSO₄ as a reflectance standard. X-ray photoelectron spectroscopy (XPS) measurements were performed using a Thermo Scientific K-Alpha XPS system (Thermo Fisher Scientific, Waltham, MA, USA) equipped with a monochromatic Al K_α source.

2.3. Photocatalytic Activity

The photocatalytic activities were measured by photodegradation of methylene blue (MB, Guangzhou Chemical Reagent Factory, Guangzhou, China). The initial concentration of MB was 10 ppm (50 mL) and the amount of the photocatalyst used was 25 mg. The dispersion was magnetically stirred in the dark for several hours to achieve the adsorption/desorption equilibrium between the dye and the photocatalyst before illumination. In UV light photocatalytic experiment, two 30 W UV lamps (Philips Lighting Co, Eindhoven, The Netherlands) were used as light source. The light intensity was 25 mW·cm⁻². Visible light photocatalytic activities were measured under white-light LED (5 W, PCX-50C, Beijing perfectlight technology co. LTD, Beijing, China). At given irradiation time intervals, 4 mL of the suspensions were collected and centrifuged. The degraded solutions of MB were analyzed by a UV-2401PC photometer (Shimadzu, Kyoto, Japan).

2.4. Time-Resolved IR Measurement

Electron decay signals were recorded by a Nicolet 8700 FTIR spectrometer with the InSb detector (Thermo Nicolet Corp., Madison, WI, USA). The frequency was 25 MHz and the scanning range is 1850 cm⁻¹ to 7400 cm⁻¹. The sample was photoexcited by 355 nm laser of 10 ns pulse from third harmonic generation of a Q-switched Nd: YAG laser (Labeit, Beijing, China). The pulse energy and frequency was tuned to 4 mJ and 10 Hz, respectively.

3. Results

3.1. Characterizations

The crystalline structures of as-prepared samples were investigated by XRD measurements. The XRD patterns of MTiO₂/Ala-DDA and MTiO₂/DDA (Figure 1) show peaks of 2θ values at 25.3°, 37.9°, 48.0°, 54.6°, 62.7°, 75.2°, and 82.7°, which correspond to (101), (004), (200), (211), (204), (215), and (224) crystallographic planes of anatase TiO₂ (JCPDS, No. 65-5714), respectively. No peak attributed to other phases was observed indicates the formation of pure anatase. However, MTiO₂/Ala shows an extra peak at 2θ = 30.81°, which corresponds to the (121) crystallographic plane of brookite (JCPDS, No. 03-0380). The amount of anatase and brookite phase is 79% and 21%, respectively, calculated from the intensities of two peaks: (101) and (121) plane [19]. This indicates that L-alanine acid is the key role in the phase transition from anatase into brookite. But when L-alanine acids and dodecylamine were simultaneously added, only anatase phase was obtained. It is suggested that the existence of dodecylamine make TiO₂ more inclined to maintain the structure of anatase.

Figure 2 shows the nitrogen adsorption–desorption isotherms and BJH pore size distribution plots (inset to Figure 2) for as-prepared samples. All examples exhibited type-IV isotherm, which is characteristic of mesoporous materials, but there are significant differences in the isotherm for each sample. The isotherms of MTiO₂/Ala and MTiO₂/DDA are intermediate between typical H1 and H2 type hysteresis loop, and the pore size distributions consists of single narrow peaks. It is implied that the materials have very uniform pore channels in the mesoporous region. The isotherm of MTiO₂/Ala-DDA shows slightly resembles H3 type hysteresis loop, and the pore size distribution is broad. This associated with aggregates of plate like particles giving rise to slit like pores [20]. Using the BJH method and the desorption branch of the nitrogen isotherm, the average pore size of MTiO₂/Ala-DDA, MTiO₂/DDA and MTiO₂/Ala is 11.8, 5.0, and 5.7 nm, respectively. The BET specific surface areas of MTiO₂/Ala-DDA, MTiO₂/DDA, and MTiO₂/Ala are 97.2, 110.1, and 96.4 m²·g⁻¹, respectively.

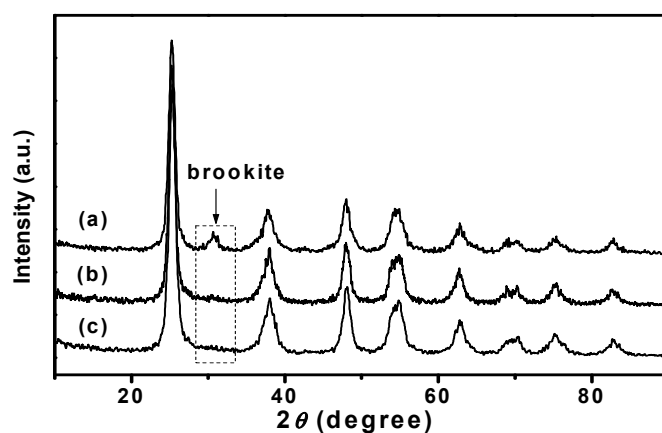


Figure 1. Patterns for (a) MTiO_2/Ala , (b) MTiO_2/DDA , and (c) $\text{MTiO}_2/\text{Ala-DDA}$.

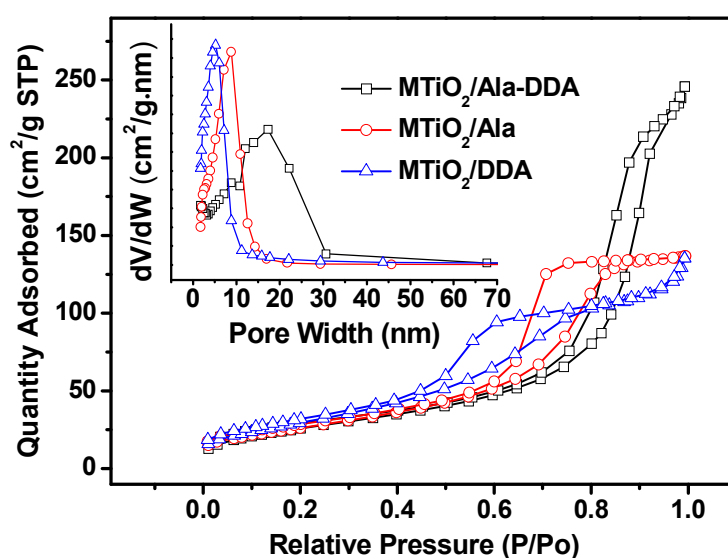


Figure 2. N_2 -sorption isotherms and pore size distribution curves (inset) of as-prepared samples.

The morphology and crystal structure of the samples were performed by SEM and TEM. Figure 3a shows the SEM image of $\text{MTiO}_2/\text{Ala-DDA}$; a number of TiO_2 spheres with diameters in the range of 300 to 500 nm were observed. As shown in Figure S1a,b, the normal distribution of $\text{MTiO}_2/\text{Ala-DDA}$ from 100 nm to 700 nm in diameter is consistent to the results from SEM images. Meanwhile, the irregular distribution above 700 nm should be attributed to different aggregation level of the particles. Figure 3b,c shows the TEM images of $\text{MTiO}_2/\text{Ala-DDA}$ with different magnifications. The TiO_2 spheres consisted of a large number of nanoparticles. In Figure 3d, the 0.35 nm interlayer spacings of $\text{MTiO}_2/\text{Ala-DDA}$ corresponding to the (101) plane of anatase TiO_2 can be obviously observed, revealing a well-defined crystal structure. Figure 4a shows TEM image of the MTiO_2/Ala nanocrystals. The average diameter of the nanocrystals was about 10 nm. The clear lattice fringes with lattice space of 0.35 nm and 0.29 nm presented by the high-resolution transmission electron microscopy (HRTEM) image (Figure 4b) of MTiO_2/Ala are assigned to (101) plane of anatase TiO_2 and (121) planes of brookite, respectively. These results agree well with XRD date. As shown in Figure 4c, the morphology of MTiO_2/DDA nanocomposite is also a spherical structure, indicates that DDA micelles tend to form a spherical shape [21]. In fact, DDA has been used as a neutral amine surfactant to control the growth of the nanocrystals because of its long nonpolar carbon chain [22]. The schematic illustration for the formation of $\text{MTiO}_2/\text{Ala-DDA}$ is shown in Scheme 1.

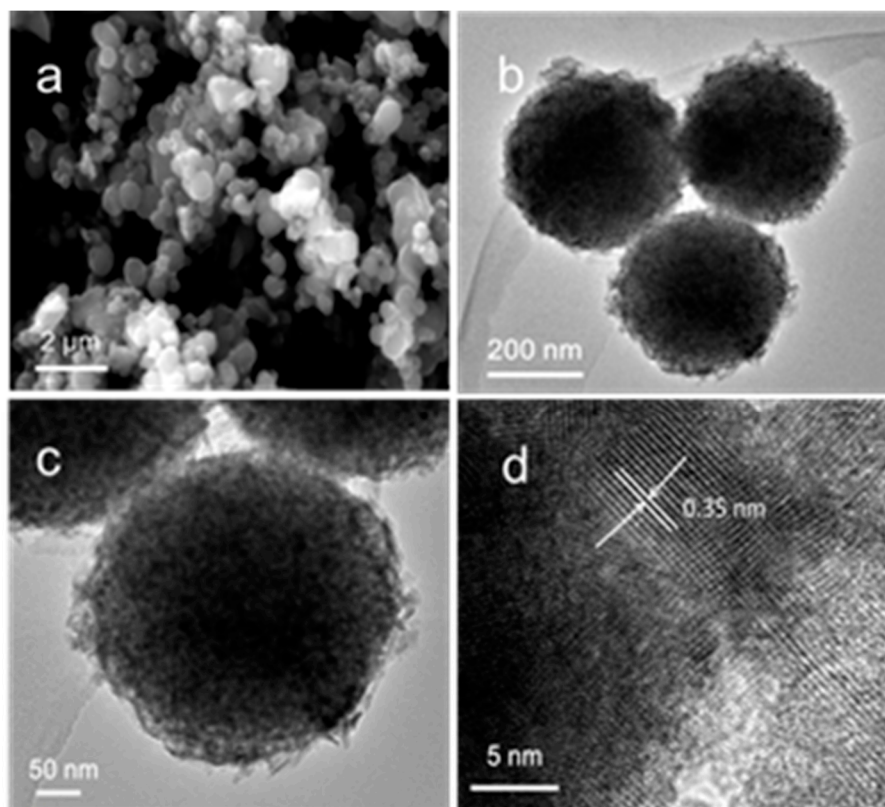


Figure 3. (a) Typical SEM, (b,c) show TEM images of $\text{MTiO}_2/\text{Ala-DDA}$ with different magnifications, and (d) shows the HTEM for $\text{MTiO}_2/\text{Ala-DDA}$ nanocrystallinity.

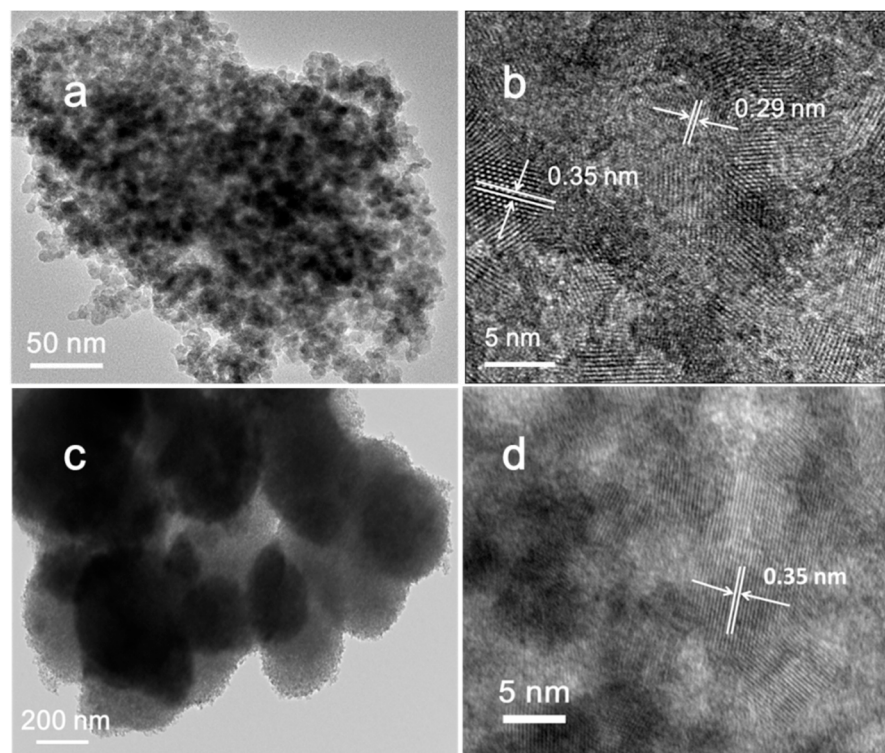
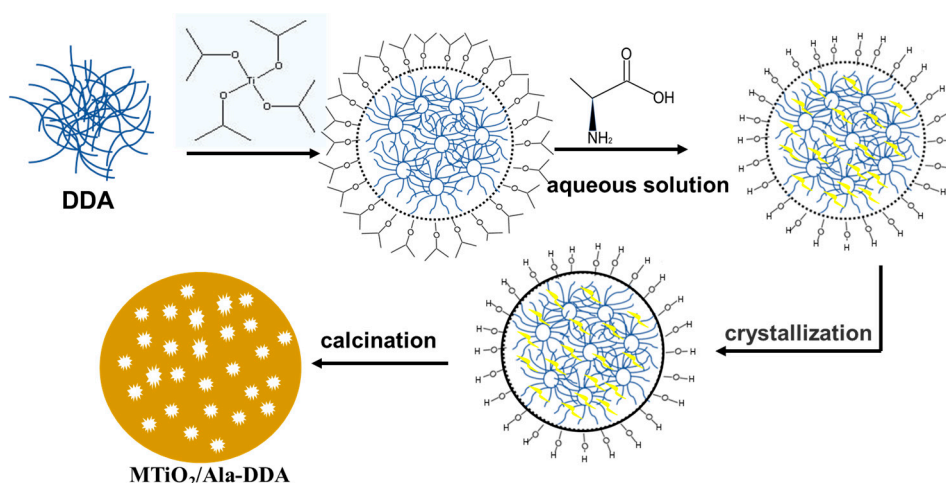


Figure 4. (a) TEM and (b) HTEM images of MTiO_2/DDA . (c) TEM and (d) HTEM images of MTiO_2/Ala .



Scheme 1. Schematic illustration for the formation of $\text{MTiO}_2/\text{Ala-DDA}$.

As shown in Figure 5, the UV–Vis DRS spectra of P25 and MTiO_2/DDA exhibit the typical absorption of TiO_2 . The absorption edge for P25 and MTiO_2/DDA both can be determined to be around 400 nm, corresponding to band gap of 3.1 eV. However, $\text{MTiO}_2/\text{Ala-DDA}$ and MTiO_2/Ala exhibit enhanced absorption in visible light region, in accordance with the colour of beige and pale yellow, respectively. Moreover, the absorption intensity of $\text{MTiO}_2/\text{Ala-DDA}$ in the visible light region is much stronger than that of MTiO_2/Ala . These results indicate that $\text{MTiO}_2/\text{Ala-DDA}$ may be doped with other elements or has special structure.

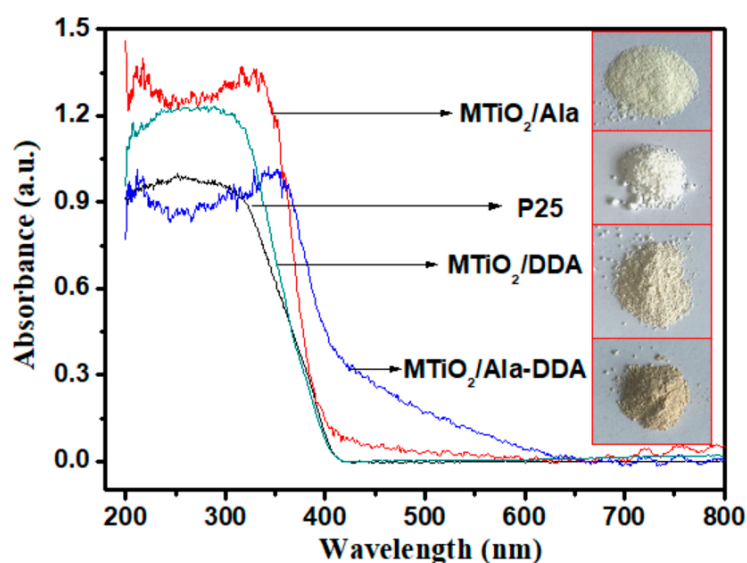


Figure 5. UV–Vis DRS spectra of P25, $\text{MTiO}_2/\text{Ala-DDA}$, MTiO_2/DDA , and MTiO_2/Ala (inset shows digital camera photographs of samples).

The surface chemical composition and chemical states of the as-prepared samples were analyzed by XPS. As shown in Figure 6, N 1s core level peak at ~ 400 eV was observed for $\text{MTiO}_2/\text{Ala-DDA}$ and MTiO_2/Ala , whereas no N 1s signals were detected on the surface of MTiO_2/DDA . The N 1s core level of N-doped TiO_2 at ~ 400 eV should be attributed to N–O bonding (i.e., Ti–O–N) [23]. Although there are some disputes for N 1s peak alone at 399–400 eV and assigned it as N–O bonding [2]. The molecular N_2 is not chemisorbed on metal oxides like TiO_2 at room temperature. So, it is suggested that nitrogen was successfully doped in TiO_2 lattice for $\text{MTiO}_2/\text{Ala-DDA}$ and MTiO_2/Ala , consistent with the results of UV–Vis diffuse reflectance spectroscopy.

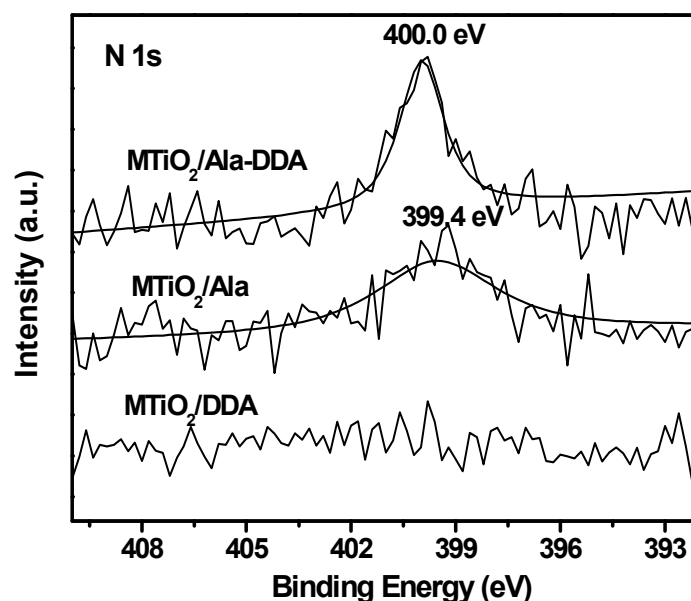


Figure 6. X-ray photoelectron spectroscopy (XPS) N 1s spectra of MTiO₂/Ala-DDA, MTiO₂/Ala, and MTiO₂/DDA.

Figure 7a shows that all samples had octahedrally coordinated Ti species with a Ti 2p_{3/2} peak, which was situated at lower binding energy (458.6 eV). It is interesting that MTiO₂/Ala-DDA exhibited another contribution at higher binding energy (~459.7 eV), which is the fingerprint of tetrahedrally coordinated Ti (IV) [24,25]. The high-energy shift of Ti 2p_{3/2} indicated change in coordination from octahedral to tetrahedral. The tetrahedral Ti⁴⁺ species was confirmed to be an intermediate in the phase transformation from anatase to rutile [15], which is usually prepared in zeolite cavities or dispersed onto silica substrate [26,27]. The results of XRD shows that in the presence of only L-alanine acids lead to the formation of anatase and brookite structure, whereas in the presence of both L-alanine acids and dodecylamine, only the anatase phase were obtained. Therefore, tetrahedral Ti⁴⁺ species with MTiO₂/Ala-DDA may be generated in the process of phase transformation from brookite to anatase. However, this is only a hypothesis and has not yet been confirmed. The formation of tetrahedrally coordinated Ti⁴⁺ species may also be due to presence of oxygen vacancies in TiO₂ [13]. The Ti⁴⁺ species brought the ligand-to-metal charge-transfer (LMCT) during the photocatalytic process and generated highly active photoexcited charge-carriers, which due to the transition from [Ti⁴⁺—O²⁻] to [Ti³⁺—O⁻]* [28,29].

The XPS spectra of the as-prepared samples in the O1s region all show two peaks at approximately 529.8 and 531.8 eV, which can be assigned to the lattice oxygen in Ti—O bond and OH groups on surfaces of the samples, respectively (Figure 7b) [16,30]. For the MTiO₂/Ala-DDA TiO₂, there is another peak at 530.6 eV perhaps belonging to O₂ molecules adsorb as O₂⁻ on the surface of TiO₂ when excess negative charge associated with oxygen vacancies [31,32]. This also further confirmed the formation of tetrahedrally coordinated Ti⁴⁺. The O₂ adsorbed on the surface of TiO₂ can produce superoxide radical groups by capturing photoinduced electrons as well as the free electrons located on oxygen vacancy states [33]. Thus, the present of TiO₄ clusters by creating oxygen vacancies may lead to increasing in activities for photocatalytic reactions [14].

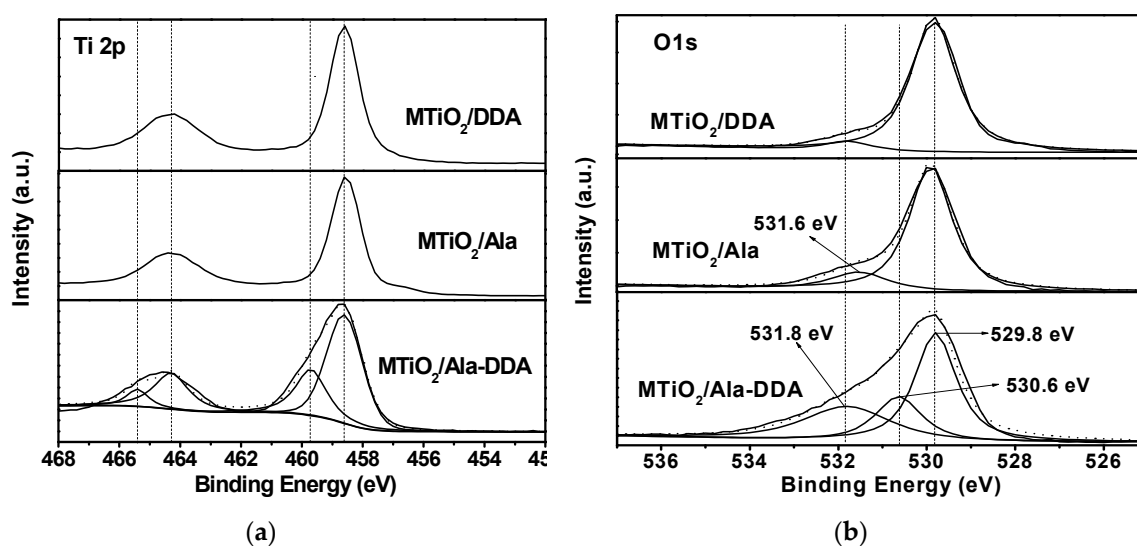


Figure 7. XPS (a) Ti 2p spectra and (b) O 1s spectra of MTiO₂/Ala-DDA, MTiO₂/DDA, and MTiO₂/Ala.

3.2. Photocatalytic Activity

The photocatalytic activities are measured by degradation of methylene blue (MB). After reaching adsorption equilibrium, the variations for maximum absorbance of MB are summarized in Figure 8a. It can be found that all samples show a little adsorption capacity for MB under dark. The adsorption yield of MB over MTiO₂/Ala-DDA, MTiO₂/DDA, MTiO₂/Ala, and P25 is 8.9%, 6.5%, 5.6%, and 8.7%, respectively. Approximately 23% of MB was photo-decomposed in the absence of a catalyst after 120 min, indicating MB is unstable under UV irradiation. However, all the catalysts exhibited specific photocatalytic activities for MB degradation under UV light. Considering the photo-decomposition of MB itself, photodegradation yield = $[(C_e - C_a - C_b)/C_e] \times 100\%$ [34]. C_e is the concentration of MB when reaching adsorption equilibrium, C_a is the concentration after photodegradation under UV light, and C_b is the decrease concentration because of the direct photolysis. The photodegradation yield of MB over MTiO₂/Ala-DDA, P25, MTiO₂/DDA, and MTiO₂/Ala is approximately 64.9%, 60.7%, 53.1%, and 19.8%, respectively.

The photocatalytic activities of the as-prepared catalysts were also evaluated under visible lights irradiation as shown in Figure 8b. Obviously, MB is much more stable under visible light. Only about 14% of MB was decomposed within 5 h without any catalyst. As expected, no photocatalytic activity was observed for P25 under visible light, and MTiO₂/DDA also showed a low photocatalytic activity. However, TiO₂/Ala-DDA and MTiO₂/Ala exhibited significant photodegradation performances under visible light. Considering the self-sensitization of MB, colorless phenol was also selected as the simulated pollutant for evaluation of photocatalytic activities over the synthesized photocatalysts. Although the photocatalytic degradation yield of phenol over all the samples is not impressive, MTiO₂/Ala-DDA still exhibits the highest activity for photocatalytic degradation of phenol (Figure S2). It is suggested the N-doping level had influence on the visible light photocatalytic activities of the TiO₂ samples. Moreover, the formation of tetrahedrally coordinated Ti⁴⁺ in TiO₂/Ala-DDA results in enhanced absorption in visible light region.

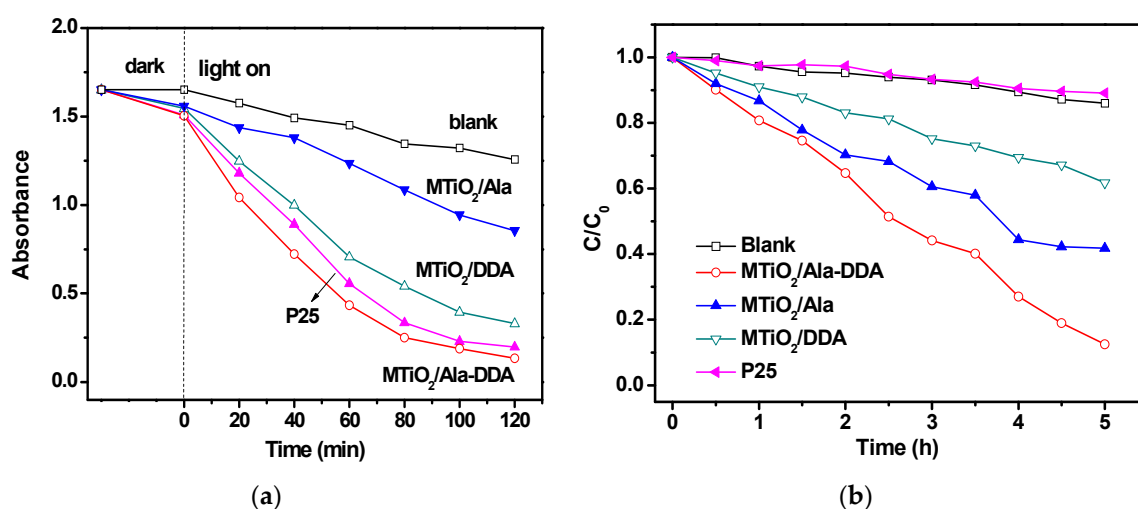


Figure 8. A comparison of the photoactivities of MTiO₂/Ala-DDA, MTiO₂/DDA, MTiO₂/Ala, and blank experiment (without catalyst) under (a) UV light and (b) visible light.

3.3. Decay Kinetics of Photogenerated Electrons

Time-resolved IR spectroscopy was demonstrated as a powerful method to accurately trace the decay of photogenerated electrons result in recombination or carrier reactions. Infrared absorption was induced by irradiation with 355 nm laser pulses. Figure 9a shows transient absorbance spectrum at 1910 cm⁻¹ of the four photocatalysts observed in the atmosphere with microsecond time delays. Obviously, the absorbance of the four catalysts at the time origin, 1 μs (time delay Δt = 1 μs), exhibited different intensities. The initial intensity of the transient absorption originates from photogenerated electrons after excitation and has a rather good relation to the number of the electrons in conduction band and/or shallowly trapped states [35,36]. Moreover, the quantity of the photogenerated charge carriers is dominated by intrinsic, bulk properties of the catalysts. MTiO₂/Ala-DDA exhibited the strongest initial absorption indicates the existence of a large amount of charge carriers. On the contrary, TiO₂/Ala appeared the lowest value of initial absorption, perhaps because brookite shows too weak infrared absorption to be detected. Shen et al. confirmed that rutile did not show any transient MIR absorption on the microsecond time scale [37]. Thus, P25 with mixed phases of anatase and rutile also appears a low initial absorption. However, the absorption intensity of MTiO₂/DDA as pure anatase is also weaker than of MTiO₂/Ala-DDA, due to formation oxygen vacancies of tetrahedral Ti⁴⁺ sites created a shallow donor state below the conduction band of MTiO₂/Ala-DDA [38]. Mid-IR light shows the electrons which are exist in the shallow traps [37]. The photogenerated charge carriers play a key role in the photocatalytic reaction as they have more opportunities to react with the surface adsorbed molecules.

Figure 9b shows the normalized absorbance decay to trace recombination for time delays of 1–400 μs. MTiO₂/Ala-DDA and P25 exhibited slower decay rate, while the decay rates of MTiO₂/DDA and MTiO₂/Ala were faster. It is indicated that the lifetime of the long-lived photogenerated electrons in the microsecond timescale for MTiO₂/Ala-DDA and P25 are much longer. For P25, the photoelectrons in anatase can transfer rapidly to rutile due to the synergism between anatase and rutile on the surface. Thus, the separation of electrons and holes is effectively realized. However, the shallow donor state produced by oxygen vacancies of tetrahedral Ti⁴⁺ sites can more effectively promote charge separation besides capturing electrons in MTiO₂/Ala-DDA. As a consequence, more long-lived photogenerated charges lead to highly efficient photocatalytic activity [39], which is inconsistent with the above photocatalytic performances under UV light.

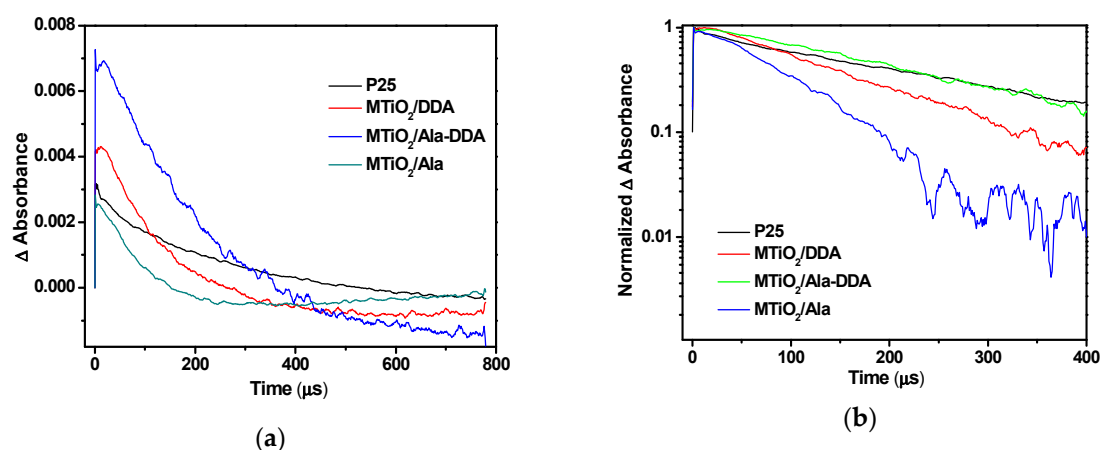
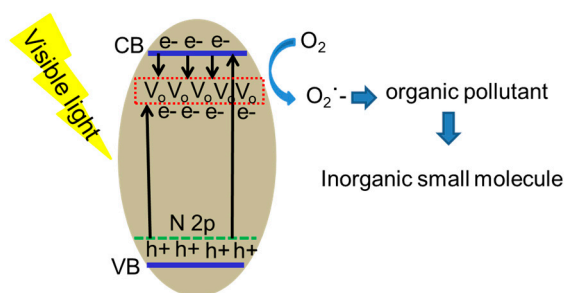


Figure 9. (a) Temporal profiles in atmosphere of transient IR absorption and (b) normalized decay curves at 1910 cm^{-1} of the four catalysts.

3.4. The Photocatalytic Mechanism

The synergistic effect of N-doping and stable oxygen vacancies in MTiO₂/Ala-DDA may contribute to the improvement of photocatalytic activity under visible light. First, the 2p orbital doped with N increases the valence band (VB) position, while the oxygen vacancy state in MTiO₂/Ala-DDA lies below the conduction band (CB), which will improve the absorption of visible light. Second, a shallow donor state was created by oxygen vacancies below the conduction band can capture a large number of photogenerated electron, thus increasing opportunities to react with the surface adsorbed molecules. Then, photogenerated electrons oxidized adsorbed oxygen in the surface of MTiO₂/Ala-DDA to superoxide radicals ($\text{O}_2^{\bullet-}$), and further mineralized organic pollutant to form inorganic small molecules, as shown in Scheme 2.



Scheme 2. Suggested mechanism for the photocatalysis of MTiO₂/Ala-DDA under visible light.

4. Conclusions

In summary, we developed a new and facile chemical process to synthesize N-doped TiO₂ nanospheres with tetrahedral Ti⁴⁺ sites in the presence of self-assembling dodecylamine and L-alanine acids. During the synthetic process, dodecylamine—a neutral surfactant—controlled the formation of TiO₂ spherical structure, while L-alanine acids provided the nitrogen source. The XPS results confirmed the existence of tetrahedral Ti⁴⁺ sites in N-doped TiO₂. The sample with tetrahedral Ti⁴⁺ sites in N-doped TiO₂ exhibited remarkable photocatalytic performance for degradation of model dye (MB) under whether UV light or visible light. The electron decay results showed that enhanced photocatalytic performance could be attributed to a large amount of photogenerated charge carriers and efficient charge separation. It is demonstrated that the shallow donor state produced by oxygen vacancies of tetrahedral Ti⁴⁺ sites can effectively promote charge separation and capturing electrons.

Supplementary Materials: The following are available online at <http://www.mdpi.com/2079-4991/9/5/698/s1>, Figure S1: Size distributions of MTiO₂/Ala-DDA, Figure S2: A comparison of photocatalytic degradation of phenol under visible light (The initial concentration of phenol was 5 ppm (50 mL) and the amount of the photocatalyst used was 25 mg).

Author Contributions: Conceptualization, Y.C. and J.W.; Data Curation, P.X.; Formal Analysis, J.L.; Funding Acquisition, J.W.; Investigation, X.L. and Y.L.; Methodology, Y.C.; Supervision, Z.Y. and J.W.; Visualization, L.J.; Writing—Original Draft, Y.C.; Writing—Review & Editing, Y.C. and J.H.

Funding: This work was supported by the National Natural Science Foundation of China (Project 21773204, 21603188, 21573193, and 21403190), Yunnan Applied Basic Research Projects (Project 2015FB106, 2016FD009, and 2016FA002), and the Scientific Research Fund of Yunnan Educational Committee (Project 2015Y010 and 2016CYH04).

Acknowledgments: The authors thank the Program for Innovation Team of Yunnan Province and Innovative Research Team (in Science and Technology) in the Universities of Yunnan Province, Key Laboratory of Advanced Materials for Wastewater Treatment of Kunming.

Conflicts of Interest: The authors declare no conflicts of interest.

References

1. Devi, L.G.; Kavitha, R. Review on modified N-TiO₂ for green energy applications under UV/visible light: Selected results and reaction mechanisms. *RSC Adv.* **2014**, *4*, 28265–28299. [[CrossRef](#)]
2. Asahi, R.; Morikawa, T.; Ohwaki, T.; Aoki, K.; Taga, Y. Visible-Light Photocatalysis in Nitrogen-Doped Titanium Oxides. *Science* **2001**, *293*, 269–271. [[CrossRef](#)]
3. Nakano, Y.; Morikawa, T.; Ohwaki, T.; Yaga, Y. Deep-level optical spectroscopy investigation of N-doped TiO₂ films. *Appl. Phys. Lett.* **2005**, *86*, 132104. [[CrossRef](#)]
4. Yu, J.; Yu, J.C.; Leung, M.K.-P.; Ho, W.; Cheng, B.; Zhao, X.; Zhao, J. Effects of acidic and basic hydrolysis catalysts on the photocatalytic activity and microstructures of bimodal mesoporous titania. *J. Catal.* **2003**, *217*, 69–78. [[CrossRef](#)]
5. Diwald, O.; Thompson, T.L.; Zubkov, T.; Goralski, E.G.; Walck, S.D.; Yates, J.T. Photochemical Activity of Nitrogen-Doped Rutile TiO₂ (110) in Visible Light. *J. Phys. Chem. B* **2004**, *108*, 6004–6008. [[CrossRef](#)]
6. Prokes, S.M.; Gole, J.L.; Chen, X.; Burda, C.; Carlos, W.E. Defect-Related Optical Behavior in Surface Modified TiO₂ Nanostructures. *Adv. Funct. Mater.* **2005**, *15*, 161–167. [[CrossRef](#)]
7. Cho, S.; Ahn, C.; Park, J.; Jeon, S. 3D nanostructured N-doped TiO₂ photocatalysts with enhanced visible absorption. *Nanoscale* **2018**, *10*, 9747–9751. [[CrossRef](#)] [[PubMed](#)]
8. Jagadale, T.C.; Takale, S.P.; Sonawane, R.S.; Joshi, H.M.; Patil, S.I.; Kale, B.B.; Ogale, S.B. N-Doped TiO₂ Nanoparticle Based Visible Light Photocatalyst by Modified Peroxide Sol–Gel Method. *J. Phys. Chem. C* **2008**, *12*, 14595–14602. [[CrossRef](#)]
9. Chemseddine, A.; Moritz, T. Nanostructuring titania: Control over nanocrystal structure, size, shape, and organization. *Eur. J. Inorg. Chem.* **1999**, *2*, 235–245. [[CrossRef](#)]
10. Kanie, K.; Sugimoto, T. Shape control of anatase TiO₂ nanoparticles by amino acids in a gel–sol system. *Chem. Commun.* **2004**, 1584–1586. [[CrossRef](#)]
11. Durupthy, O.; Bill, J.; Aldinger, F. Bioinspired Synthesis of Crystalline TiO₂: Effect of Amino Acids on Nanoparticles Structure and Shape. *Cryst. Growth Des.* **2007**, *7*, 2696–2704. [[CrossRef](#)]
12. Wang, J.; Tafen, D.N.; Lewis, J.P.; Hong, Z.; Manivannan, A.; Zhi, M.; Li, M.; Wu, N. Origin of Photocatalytic Activity of Nitrogen-Doped TiO₂ Nanobelts. *J. Am. Chem. Soc.* **2009**, *131*, 12290–12297. [[CrossRef](#)]
13. Batzill, M.; Morales, E.H.; Diebold, U. Influence of Nitrogen Doping on the Defect Formation and Surface Properties of TiO₂ Rutile and Anatase. *Phys. Rev. Lett.* **2006**, *96*, 026103. [[CrossRef](#)]
14. Wu, Q.; Zheng, Q.; Krol, R. van de Creating Oxygen Vacancies as a Novel Strategy To Form Tetrahedrally Coordinated Ti⁴⁺ in Fe/TiO₂ Nanoparticles. *J. Phys. Chem. C* **2012**, *116*, 7219–7226. [[CrossRef](#)]
15. Li, G.; Dimitrijevic, N.M.; Chen, L.; Nichols, J.M.; Rajh, T.; Gray, K.A. The Important Role of Tetrahedral Ti⁴⁺ Sites in the Phase Transformation and Photocatalytic Activity of TiO₂ Nanocomposites. *J. Am. Chem. Soc.* **2008**, *130*, 5402–5403. [[CrossRef](#)]
16. Wang, Y.; Feng, C.; Zhang, M.; Yang, J.; Zhang, Z. Enhanced visible light photocatalytic activity of N-doped TiO₂ in relation to single-electron-trapped oxygen vacancy and doped-nitrogen. *Appl. Catal. B* **2010**, *100*, 84–90. [[CrossRef](#)]

17. Zhang, Z.; Long, J.; Xie, X.; Zhuang, H.; Zhou, Y.; Lin, H.; Yuan, R.; Dai, W.; Ding, Z.; Wang, X.; et al. Controlling the synergistic effect of oxygen vacancies and N dopants to enhance photocatalytic activity of N-doped TiO₂ by H₂ reduction. *Appl. Catal. A* **2012**, *425–426*, 117–124. [[CrossRef](#)]
18. Yao, W.; Fang, H.; Ou, E.; Wang, J.; Yan, Z. Highly efficient catalytic oxidation of cyclohexane over cobalt-doped mesoporous titania with anatase crystalline structure. *Catal. Comm.* **2006**, *7*, 387–390. [[CrossRef](#)]
19. Xu, H.; Zhang, L. Controllable One-Pot Synthesis and Enhanced Photocatalytic Activity of Mixed-Phase TiO₂ Nanocrystals with Tunable Brookite/Rutile Ratios. *J. Phys. Chem. C* **2009**, *113*, 1785–1790. [[CrossRef](#)]
20. Yu, X.; Yu, J.; Cheng, B.; Jaroniec, M. Synthesis of Hierarchical Flower-like AlOOH and TiO₂/AlOOH Superstructures and their Enhanced Photocatalytic Properties. *J. Phys. Chem. C* **2009**, *113*, 17527–17535. [[CrossRef](#)]
21. Zhuang, J.; Tian, Q.; Zhou, H.; Liu, Q.; Liu, P.; Zhong, H. Hierarchical porous TiO₂@C hollow microspheres: One-pot synthesis and enhanced visible-light photocatalysis. *J. Mater. Chem.* **2012**, *22*, 7036–7042. [[CrossRef](#)]
22. Pan, B.F.; He, R.; Gao, D.X.; Zhang, Y.F. Study on growth kinetics of CdSe nanocrystals in oleic acid/dodecylamine. *J. Cryst. Growth* **2006**, *286*, 318–323. [[CrossRef](#)]
23. Sato, S.; Nakamura, R.; Abe, S. Visible-light sensitization of TiO₂ photocatalysts by wet-method N doping. *Appl. Catal. A* **2005**, *284*, 131–137. [[CrossRef](#)]
24. Garbassi, F.; Balducci, L. Preparation and characterization of spherical TiO₂-SiO₂ particles. *Micropor. Mesopor. Mater.* **2001**, *47*, 51–59. [[CrossRef](#)]
25. Petrik, I.S.; Krylova, G.V.; Kelyp, O.O.; Lutsenko, L.V.; Smirnova, N.P.; Oleksenko, L.P. XPS and TPR study of sol-gel derived M/TiO₂ powders (M=Co, Cu, Mn, Ni). *Chem. Phys. Tech. Surf.* **2015**, *6*, 179–189.
26. Yamashita, H.; Ichihashi, Y.; Zhang, S.G.; Matsumura, Y.; Souma, Y.; Tatsumi, T.; Anpo, M. Photocatalytic decomposition of NO at 275 K on titanium oxide catalysts anchored within zeolite cavities and framework. *Appl. Surf. Sci.* **1997**, *121–122*, 305–309. [[CrossRef](#)]
27. Anpo, M.; Takeuchi, M.; Ikeue, K.; Dohshi, S. Design and development of titanium oxide photocatalysts operating under visible and UV light irradiation. - The applications of metal ion-implantation techniques to semiconducting TiO₂ and Ti/zeolite catalysts. *Curr. Opin. Solid State Mater. Sci.* **2002**, *6*, 381–388. [[CrossRef](#)]
28. Anpo, M.; Thomas, J.M. Single-site photocatalytic solids for the decomposition of undesirable molecules. *Chem Commun.* **2006**, 3273–3278. [[CrossRef](#)] [[PubMed](#)]
29. Anpo, M.; Kim, T.-H.; Matsuoka, M. The design of Ti-, V-, Cr-oxide single-site catalysts within zeolite frameworks and their photocatalytic reactivity for the decomposition of undesirable molecules—The role of their excited states and reaction mechanisms. *Catal. Today* **2009**, *142*, 114–124. [[CrossRef](#)]
30. Li, H.; Li, J.; Huo, Y. Highly Active TiO₂N Photocatalysts Prepared by Treating TiO₂ Precursors in NH₃/Ethanol Fluid under Supercritical Conditions. *J. Phys. Chem. B* **2006**, *110*, 1559–1565. [[CrossRef](#)] [[PubMed](#)]
31. Balamurugan, J.; Thangamuthu, R.; Pandurangan, A. Growth of carbon nanotubes over transition metal loaded on Co-SBA-15 and its application for high performance dye-sensitized solar cells. *J. Mater. Chem. A* **2013**, *1*, 5070–5080. [[CrossRef](#)]
32. Thompson, T.L.; Yates, J.T. Surface Science Studies of the Photoactivation of TiO₂ New Photochemical Processes. *Chem. Rev.* **2006**, *106*, 4428–4453. [[CrossRef](#)]
33. Pan, X.; Yang, M.; Fu, X.; Zhang, N.; Xu, Y. Defective TiO₂ with oxygen vacancies: Synthesis, properties and photocatalytic applications. *Nanoscale* **2013**, *5*, 3601–3614. [[CrossRef](#)]
34. Wu, Y.; Liu, S.; Zuo, Y.; Li, J.; Wang, J. Photodegradation of some dyes over Ce/FSM-16 catalyst under solar light. *Catal. Lett.* **2007**, *119*, 245–251. [[CrossRef](#)]
35. Rothenberger, G.; Moser, J.; Graetzel, M.; Serpone, N.; Sharma, D.K. Charge carrier trapping and recombination dynamics in small semiconductor particles. *J. Am. Chem. Soc.* **1985**, *107*, 8054–8059. [[CrossRef](#)]
36. Takeshita, K.; Sasaki, Y.; Kobashi, M.; Tanaka, Y.; Maeda, S.; Yamakata, A.; Ishibashi, T.; Onishi, H. Photophysics and electron dynamics in dye-sensitized semiconductor film studied by time-resolved mid-IR spectroscopy. *J. Phys. Chem. B* **2003**, *107*, 4156–4161. [[CrossRef](#)]
37. Shen, S.; Wang, X.; Chen, T.; Feng, Z.; Li, C. Transfer of Photoinduced Electrons in Anatase-Rutile TiO₂ Determined by Time-Resolved Mid-Infrared Spectroscopy. *J. Phys. Chem. C* **2014**, *118*, 12661–12668. [[CrossRef](#)]

38. Panayotov, D.A.; Morris, J.R. Thermal Decomposition of a Chemical Warfare Agent Simulant (DMMP) on TiO₂: Adsorbate Reactions with Lattice Oxygen as Studied by Infrared Spectroscopy. *J. Phys. Chem. C* **2009**, *113*, 15684–15691. [[CrossRef](#)]
39. Chen, T.; Feng, Z.H.; Wu, G.P.; Shi, J.Y.; Ma, G.J.; Ying, P.L.; Li, C. Mechanistic Studies of Photocatalytic Reaction of Methanol for Hydrogen Production on Pt/TiO₂ by in situ Fourier Transform IR and Time-Resolved IR Spectroscopy. *J. Phys. Chem. C* **2007**, *111*, 8005–8014. [[CrossRef](#)]



© 2019 by the authors. Licensee MDPI, Basel, Switzerland. This article is an open access article distributed under the terms and conditions of the Creative Commons Attribution (CC BY) license (<http://creativecommons.org/licenses/by/4.0/>).